Journal of Geophysics and Engineering, 2026, **23**(4), 1434–1449
https://doi.org/10.1093/jge/gxag044
Advance access publication date: 30 April 2026
Research Article

OXFORD

A robust three-dimensional inversion scheme for controlled-source audio-frequency magnetotelluric data

Shengtao Wang[1,2], Changhong Lin[1,2,*], Gianluca Fiandaca[3], Dongyue Xin[1,2]

[1]State Key Laboratory of Deep Earth Exploration and Imaging, School of Geophysics and Information Technology, China University of Geosciences (Beijing), 29 Xueyuan Road, Haidian District, Beijing 100083, China
[2]School of Geophysics and Information Technology, China University of Geosciences (Beijing), 29 Xueyuan Road, Haidian District, Beijing 100083, China
[3]Department of Earth Sciences, University of Milan, Via Sandro Botticelli 23, Milan 20133, Italy
*Corresponding author. State Key Laboratory of Deep Earth Exploration and Imaging, School of Geophysics and Information Technology, China University of Geosciences (Beijing), 29 Xueyuan Road, Haidian District, Beijing 100083, China. E-mail: linchh@cugb.edu.cn

Abstract

Controlled-source audio-frequency magnetotelluric (CSAMT) methods are widely employed in geothermal, mineral, and groundwater exploration due to their capability to image subsurface resistivity distributions. The application of three-dimensional (3D) inversion techniques to process CSAMT field data and recover 3D resistivity models has become increasingly common. However, traditional 3D inversion schemes often exhibit low computational efficiency, poor convergence, and limited accuracy in large-scale applications, particularly when Dirichlet boundary conditions are used. To address these challenges, a robust inversion scheme is evaluated, which integrates a 3D nonlinear conjugate gradient framework with four key strategies—(i) short-offset acquisition, (ii) a perfectly matched layer-based forward modeling approach, (iii) a cooling strategy for the regularization factor, and (iv) confinement of the inversion domain to high-sensitivity regions—to enhance model accuracy, numerical stability, and computational efficiency. Synthetic tests demonstrate that the proposed scheme achieves faster convergence and more reliable resistivity recovery, with improved resistivity values and anomaly boundaries compared to conventional Dirichlet-based methods. A field case study in the Yanqing geothermal area further illustrates its practical advantages, producing resistivity images that better align with borehole and geologic information, with significantly improved recovery of deep targets and reduced data misfit.

Keywords controlled-source audio-frequency magnetotellurics; perfectly matched layer; 3D inversion; data sensitivity analysis; nonlinear conjugate gradient (NLCG)

1. Introduction

Controlled-source audio-frequency magnetotelluric (CSAMT) methods have found extensive applications in geothermal exploration, mineral prospecting, and groundwater detection (Boerner *et al.* 1993; Pellerin *et al.* 1996; Wannamaker 1997; Unsworth *et al.* 2000; Chen & Yan 2005; Lin *et al.* 2012; Kouadio *et al.* 2020). Recent advances in forward modeling and inversion techniques have led to the development of various three-dimensional (3D) CSAMT inversion algorithms (Lin *et al.* 2012; Jia & Groom 2013; Wang *et al.* 2017; Chen *et al.* 2020; Mackie *et al.* 2020), which are now being increasingly employed in the interpretation of CSAMT field data (Lin *et al.* 2018; Cao *et al.* 2021; Li *et al.* 2025). However, significant challenges remain in applying 3D inversion, particularly for large-scale field CSAMT datasets.

In typical CSAMT surveys, the transmitter is placed 5–10 km from the measurement area (Nabighian 1991; Lei *et al.* 2016), which requires the inversion domain to encompass both the survey zone and the remote source, significantly increasing the model size in 3D inversion. Moreover, accurate forward modeling necessitates fine spatial discretization, leading to a substantially larger number of grid cells compared to one-dimensional and two-dimensional cases. Most CSAMT forward modeling and inversion schemes adopt Dirichlet boundary conditions, which demand an extended computational domain to suppress artificial reflections and effectively absorb outgoing waves. In large-scale CSAMT applications, the total number of model cells can reach several hundred thousand or even exceed one million, which poses a significant challenge to computational efficiency (Kelbert *et al.* 2014; Lin *et al.* 2018). To mitigate these challenges, several strategies have been proposed in recent studies. Parallel computing techniques, such as Message Passing Interface (MPI)-based implementations (Kelbert *et al.* 2014; He *et al.* 2019), have been employed to accelerate the inversion process. A short-offset acquisition scheme has been introduced to reduce the spatial extent of the inversion domain (Wang & Lin 2025), and cooling strategies for the regularization parameter have been applied to improve inversion convergence (Haber *et al.* 2000; Kong *et al.* 2021). In addition, perfectly matched layer (PML) boundary conditions have been used to enhance forward modeling efficiency (Li *et al.* 2018); however, they

Received: 28 October 2025. **Revised:** 28 January 2026. **Accepted:** 1 March 2026

have not yet been integrated into the CSAMT inversion process. Despite these efforts, existing measures remain insufficient for efficiently addressing the computational demands of large-scale 3D CSAMT inversion problems.

Gradient-based optimization algorithms remain the dominant strategy for 3D CSAMT inversion (Commer & Newman 2009; Kelbert *et al.* 2014; Lin *et al.* 2018; Chen *et al.* 2020; Peng *et al.* 2023). Although these methods perform well under ideal conditions, their convergence may deteriorate in large-scale 3D CSAMT applications due to the presence of relatively strong but unevenly distributed model parameter gradients in the extended regions imposed by Dirichlet boundary conditions. Moreover, updating resistivity values in these regions during inversion can compromise the accuracy of recovered models within the target zone. To address these issues, constrained inversion approaches using geological or borehole data (Moorkamp *et al.* 2011; Di *et al.* 2020) has been proposed. However, in most practical exploration scenarios, such prior information is often unavailable.

A robust nonlinear conjugate gradient (NLCG) inversion scheme based on PML-based forward modeling is proposed, specifically designed for large-scale 3D CSAMT inversion. In this scheme, we use short-offset acquisition to reduce the model domain and restrict the inversion domain to high-sensitivity regions. Additional modifications are introduced to further enhance the robustness of the inversion process and enhance the inversion efficiency. We validate the proposed approach using synthetic and field datasets, demonstrating its effectiveness and providing a practical pathway for efficient and accurate 3D CSAMT inversion in large-scale geophysical exploration and subsurface characterization.

2. Methods

In this section, we will describe the steps involved in the investigation: (i) the 3D modeling with PML and (ii) the robust inversion scheme.

2.1. 3D modeling with PML

For simulating CSAMT data, we developed a 3D modeling algorithm. In CSAMT forward modeling, a key challenge is the singularity of the source, which makes it difficult to represent accurately using a discrete formulation (Unsworth *et al.* 1993). To overcome this issue, we employ a decomposition strategy that separates the total electromagnetic field into primary and secondary components. These components are solved independently and then combined to obtain the total field. The primary field is computed using numerical method. The PML boundary conditions are implemented at the domain boundaries to truncate the simulation region, as illustrated in Fig. 1.

Assuming a harmonic time dependence of $e^{-j\omega t}$, the secondary electric field $\boldsymbol{E}_s$ and magnetic field $\boldsymbol{H}_s$ are described by Maxwell's equations:

$$\nabla \times \boldsymbol{E}_s = j\omega \boldsymbol{\Lambda} \cdot \mu_0 \boldsymbol{H}_s, \tag{1}$$

$$\nabla \times \boldsymbol{H}_s = \sigma \boldsymbol{\Lambda} \cdot \boldsymbol{E}_s + (\sigma - \sigma_b)\boldsymbol{\Lambda} \cdot \boldsymbol{E}_p, \tag{2}$$

where $\boldsymbol{E}_p$ is the primary electric field, σ_b denotes the background resistivity, σ is the model resistivity, ω denotes the angular frequency, μ_0 is the vacuum magnetic permeability, j is the imaginary unit, and $\boldsymbol{\Lambda}$ is referred to as the matched matrix:

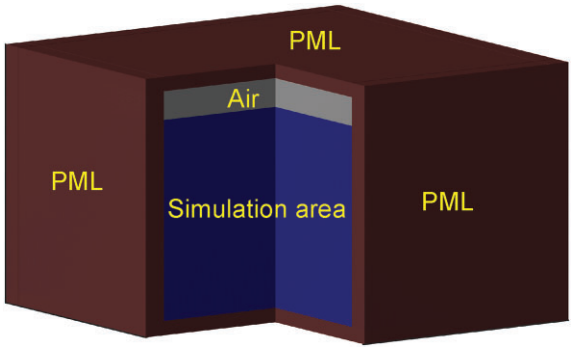

Figure 1 Schematic diagram of the spatial relationship between the PML and the simulation domain.

$$\boldsymbol{\Lambda} = \begin{bmatrix} \frac{s_y s_z}{s_x} & & \\ & \frac{s_x s_z}{s_y} & \\ & & \frac{s_x s_y}{s_z} \end{bmatrix}.$$

In the matrix $\boldsymbol{\Lambda}$, s_i (where i represents x, y, and z) can be calculated with the following (Yang *et al.* 2021):

$$s_i = \kappa_i + \frac{\sqrt{2}\gamma_i}{(\alpha_i - j)\sqrt{\omega\varepsilon_0\sigma}}, \tag{3}$$

where σ is the conductivity and can be set as the background conductivity of the model, ε_0 is vacuum permittivity, γ_i represents the PML decay factor, and κ_i and α_i are the parameters associating with the attenuation of the evanescent waves. The value of κ_i, γ_i, α_i can be calculated using the Equations following equations:

$$\kappa_i = 1 + \kappa_{max}\left(e^{\frac{h_i}{d}} - 1\right), \tag{4}$$

$$\gamma_i = \frac{\gamma_{max}}{\Delta h_i} \cdot \mu_0 \sqrt{\frac{\varepsilon_0}{\mu_0}}\left(e^{\frac{h_i}{d}} - 1\right), \tag{5}$$

$$\alpha_i = \alpha_{max}\left(e^{\left(1-\frac{h_i}{d}\right)} - 1\right), \tag{6}$$

where d represents the total PML thickness in a given direction, with the PML cell width being uniform, h_i is the distance from the center of the PML cells to the medium-PML interface, Δh_i denotes the thickness of a single PML cell. The parameters κ_{max}, γ_{max}, and α_{max} control the maximum values of κ_i, γ_i, and α_i, respectively. These parameters are crucial for the attenuation of the outgoing wave, and their optimal values—referred to as the optimal PML parameters: κ_{opt}, γ_{opt}, and α_{opt}—be selected based on a series of numerical experiments (Feng & Wang 2017).

Equations (1) and (2) are discretized using the staggered-grid finite difference method that the $\boldsymbol{H}_s$ and $\boldsymbol{E}_s$ are placed on the edges and the cell faces, resulting in the linear system $\boldsymbol{Kh} = \boldsymbol{s}$ ($\boldsymbol{K}$ is a sparse complex-symmetric matrix, $\boldsymbol{h}$ is the unknown vector composed of the secondary magnetic and $\boldsymbol{s}$ is the vector related to primary electric fields and the boundary conditions). Since the magnetic field is solved first in our study, a perfect magnetic conductor boundary condition is applied at the boundary of the PML, enforcing zero tangential components of the magnetic field (Liu *et al.* 2013).

The primary electric and magnetic fields for a uniform whole space or a layered half-space are computed using the expressions from Maxwell's equations (Ward & Hohmann 1988), incorporating the electric source term and the Hankel transform method. The

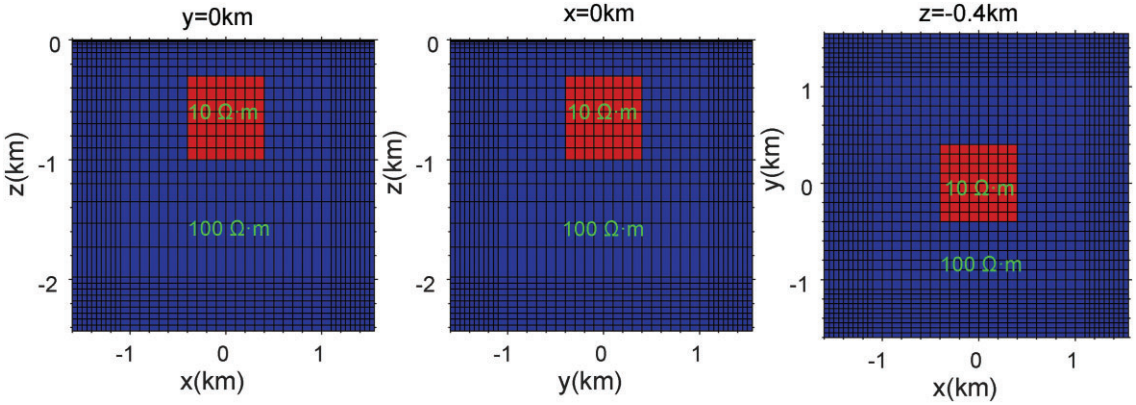

Figure 2 The model used to verify the forward modeling code. A 10 Ω m resistivity target is embedded within a 100 Ω m homogeneous background.

numerical integration method proposed by Chave (1983) is employed to ensure accurate evaluation of the integrals.

However, the introduction of PML significantly increases the condition number of the system matrix $\boldsymbol{K}$, which may lead to non-convergence when using iterative solvers. To address this, we employ the direct solver PARDISO to solve the system efficiently.

To verify the accuracy of forward modeling code, we designed a model consisting of a 10 Ω m resistivity prism embedded in a 100 Ω m homogeneous background, as illustrated in Fig. 2. The top of the target is located at a depth of 0.3 km, and its dimensions are 0.8, 0.8, and 0.7 km in the *x*-, *y*-, and *z*- directions, respectively. The coordinate origin is located directly above the target. The transmitter with a length of 2 km is positioned outside the simulation domain at coordinates (0, 6, 0) km, and 10 PML layers with a width of 50 m are implemented along the boundaries to absorb outgoing secondary fields. The model is discretized into a grid of $42 \times 42 \times 48$ cells, including the air layer and PML regions.

The optimal PML parameters, κ_{opt}, γ_{opt}, and α_{opt} were determined through a series of numerical experiments. The test model in Fig. 2 was used to illustrate the procedure. First, the frequency range from 8192 to 0.125 Hz was selected to simulate the CSAMT responses. To reduce computational cost, we select a subset of frequencies—4096, 128, 16, 2, and 0.125 Hz—for determining the optimal PML parameters: κ_{opt}, γ_{opt}, and α_{opt}. Second, the search ranges for κ_{max}, γ_{max}, and α_{max} are selected according to empirical experience as $[-5.17, 12.06]$, $[1, 20]$, and $[1, 200]$, respectively. Third, the secondary fields are computed for various PML parameter combinations. In our study, the secondary magnetic field component in the *y*-direction (H_{sy}) is used to evaluate the absorption performance of each parameter set, as the secondary electric field is directly derived from the secondary magnetic field, and the apparent resistivity calculation depends on the *y*-component of the magnetic field. The results computed with Dirichlet boundary conditions are used as reference to calculate the reflection error at each node in the simulation domain, using the following (Correia & Jin 2005):

$$error_{reflection} = 20\log_{10}\left|\frac{abs\left(H_{syi}\right) - abs\left(H_{syi}^{ref}\right)}{\max\left(abs\left(H_{syi}^{ref}\right)\right)}\right|, \qquad (7)$$

where i denotes the index of a node within the modeling region grid, H_{syi} is the secondary field calculated from the PML boundary condition, and H_{syi}^{ref} is the reference secondary field calculated from the Dirichlet boundary condition. The optimal PML parameters are those that minimize the reflection error. Figure 3 displays the minimum reflection errors for different parameter sets at selected frequencies. The optimal values were found to be $\kappa_{opt} = 2.55$, $\gamma_{opt} = 3.62$ and $\alpha_{opt} = 186.27$, yielding a minimum reflection error of –49.61 dB.

Using these parameters, we calculated the electromagnetic responses over the full frequency range from 8192 to 0.125 Hz. Figure 4d shows the minimum reflection error at each frequency across the domain, with the largest error being –48.58 dB at 10 Hz, and the smallest error –102.34 dB at 8192 Hz. These results confirm that the PML implementation achieves excellent absorption performance, with reflection errors consistently below –40 dB (Gedney 1996).

Figure 4a–c compares H_{sy} at 0.125 Hz along the *x*-, *y*-, and *z*-directions through the point (0, 0, and 0) km, computed using PML and Dirichlet boundary conditions. Within the modeling domain, the results for H_{sy} are nearly identical. In the PML region, H_{sy} gradually decreases to zero along the *x*- and *z*- directions, demonstrating effective wave absorption. Figure 4e–h presents the apparent resistivity and phase at the origin (0, 0, and 0) km calculated using the two boundary conditions, along with the relative error for apparent resistivity and the absolute error for phase. The differences are minimal, with the relative error of apparent resistivity within 0.5% and the absolute phase error within 0.5°, indicating the high accuracy and reliability of our forward modeling code.

2.2. The robust NLCG inversion scheme

The goal of the inverse problem is to estimate a subsurface electrical resistivity model that best explains the observed CSAMT data. Mathematically, this is achieved by minimizing the following objective function. To mitigate the non-uniqueness of the inversion results, the regularization concept proposed by Tikhonov & Arsenin (1977) is incorporated into the objective function:

$$\Phi(\boldsymbol{m}) = \left(\boldsymbol{d}^{obs} - \boldsymbol{F}(\boldsymbol{m})\right)^T \boldsymbol{V}^{-1}\left(\boldsymbol{d}^{obs} - \boldsymbol{F}\left(\boldsymbol{m}\right)\right) + \lambda(\boldsymbol{m}_0 - \boldsymbol{m})^T \boldsymbol{L}^T \boldsymbol{L}\,(\boldsymbol{m}_0 - \boldsymbol{m}), \qquad (8)$$

and its gradient is

$$\mathbf{g}\,(\boldsymbol{m}) = -2\boldsymbol{J}^T\boldsymbol{q} + 2\lambda\boldsymbol{L}^T\boldsymbol{L}\,(\boldsymbol{m}_0 - \boldsymbol{m}), \qquad (9)$$

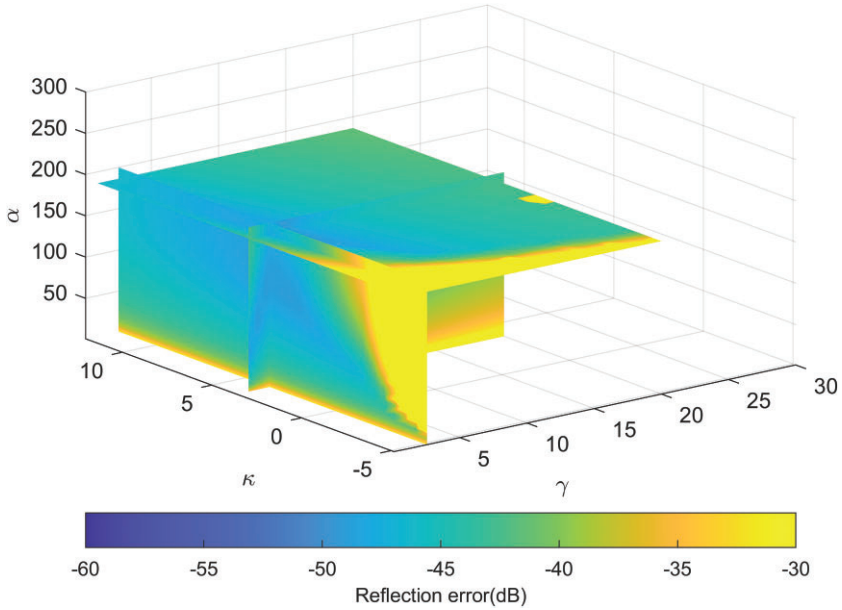

Figure 3 The minimum reflection errors for different parameter sets at selected frequencies.

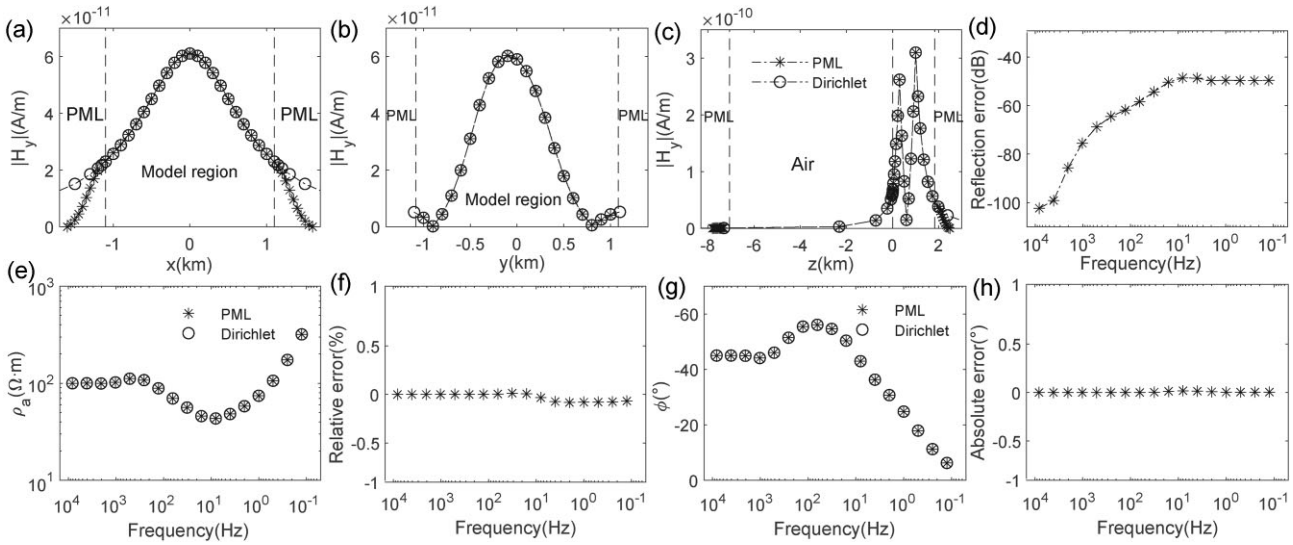

Figure 4 Comparison of results obtained using PML and Dirichlet boundary conditions (a), (b), and (c). The H_{sy} at 0.125 Hz along the *x*-, *y*-, and *z*-directions passing through the point (0, 0, and 0) km (d). Minimum reflection error within the simulation domain at each frequency ranging from 8192 to 0.125 Hz (e) and (g). Apparent resistivity and phase at the origin (0, 0, and 0) km calculated under the two boundary conditions (f) and (h). Corresponding relative errors in apparent resistivity and absolute errors in phase, respectively.

where $\boldsymbol{d}^{obs}$ represents the observed apparent resistivity or phase data at each frequency and sounding location, $\boldsymbol{F}(\boldsymbol{m})$ denotes the forward modeling operator, and $\boldsymbol{V}$ is a diagonal matrix containing the estimated variances of the observed data. The regularization factor λ controls the trade-off between data misfit and model regularity. $\boldsymbol{L}$ represents a discrete Laplacian operator based on second-order differences, $\boldsymbol{m}$ denotes the model parameters to be estimated, $\boldsymbol{m}_0$ represents the a priori model, the Jacobian matrix $\boldsymbol{J}$ represents the sensitivity of the forward response with respect to the model, and $\boldsymbol{q} = \boldsymbol{V}^{-1}(\boldsymbol{d}^{obs} - \boldsymbol{F}(\boldsymbol{m}))$ is the data-weighted residual.

Considering that Gauss–Newton and Occam inversion strategies typically require the computation of Jacobian-related information, which may entail substantial memory costs for large-scale problems, a preconditioned Polak–Ribiere NLCG scheme (Nocedal & Wright 2006) is adopted in this study for CSAMT data inversion. Newman & Alumbaugh (2000) demonstrated that the NLCG method is well suited for large-scale electromagnetic inversion problems. During the inversion process, the termination criterion is satisfied when the root-mean-square (RMS) misfit of the current iteration falls below the target RMS, or when the maximum number of iterations is reached.

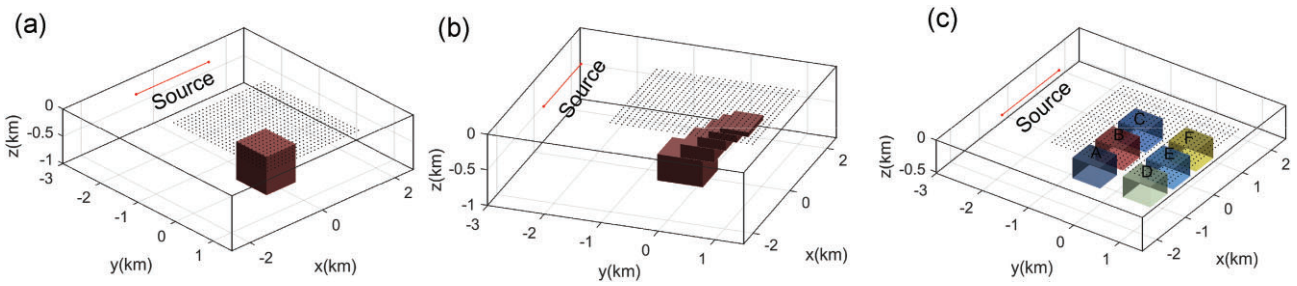

Figure 5 Synthetic models. (a)–(c) Models 1–3. In (a) and (b), the target bodies represent a resistivity of 10 Ω m embedded in a 100 Ω m homogeneous background. In (c), prisms labeled A to F correspond to targets with resistivities of 1000, 1, 500, 50, 300, and 10 Ω m, respectively. The background resistivity is 100 Ω m. The source is shown as a line, and the survey stations are indicated by discrete measurement points in (a)–(c).

In conventional CSAMT inversion, Dirichlet boundary conditions are commonly used to truncate the forward-modeling domain. However, this approach introduces numerous model cells in non-target regions, which not only reduces the efficiency of both forward modeling and inversion but also causes the extended regions—added solely for applying the boundary conditions—to dilute the data sensitivity, thereby decreasing the inversion accuracy within the survey area.

Furthermore, although the traditional long-offset acquisition scheme (5–10 km) is unproblematic during data collection, it substantially increases the number of model cells required in forward and inversion computations, since the area between the source and the survey region must also be included in the modeling domain. These regions may still exhibit non-negligible data sensitivity, potentially influencing the inversion results in the target area. In addition, as these regions are involved in the inversion process, the mesh cannot be overly coarse in order to ensure the accuracy of forward modeling; however, refining the mesh inevitably leads to a considerable increase in computational cost for both forward modeling and inversion.

Therefore, based on the NLCG inversion scheme, four combined strategies were introduced to mitigate the aforementioned issues and enhance the stability of large-scale data inversion: (i) short-offset acquisition were employed to reduce the inversion domain; (ii) a PML-based forward modeling approach was incorporated into the inversion process; (iii) a cooling strategy for the regularization factor λ was introduced to ensure optimal inversion performance; and (iv) the inversion domain was confined to the high-sensitivity regions. In the following, these four strategies are treated in detail.

2.2.1. Short-offset acquisition

Wang & Lin (2025) showed that a shortened transmitter–receiver offset strategy (2–4 km) is effective in CSAMT exploration when appropriate offsets and operating frequencies are chosen. Short offsets reduce the number of model cells in the inversion, lowering computational cost per iteration. Importantly, they also decrease the extent of low-sensitivity regions, improving the distribution of model parameter gradients and enhancing the stability of NLCG search directions.

2.2.2. The forward modeling with PML

Forward modeling with Dirichlet boundary conditions suffers from accuracy loss and reduced efficiency in the extended boundary regions. To overcome this problem, we adopt a PML-based forward modeling approach, which eliminates the need for extended regions and avoids their negative influence on inversion. A method for selecting optimal PML parameters has been developed for specific models. However, because model parameters are continuously updated during inversion, the effectiveness of these parameters in iterative inversion requires further investigation. This concern will be analyzed in detail in the Inversion Results section.

2.2.3. Cooling strategy for λ

Fixed regularization factors can hinder further reduction of data misfit in late iterations (Kong *et al.* 2021). To mitigate this, we introduce a dynamic cooling strategy: when the absolute difference between consecutive RMS misfits falls below a small tolerance (e.g. 2e-3), λ is divided by a predetermined factor (>1). NLCG inversion is then reinitialized, ensuring convergence towards an optimal solution and improving the final data fit.

2.2.4. Optimal inversion domain

In our robust inversion scheme, the size of the inversion domain can be manually specified. Based on the initial data sensitivity, which quantifies how strongly the observed responses react to variations in model parameters (Christensen 2014), model updates are restricted to regions of high sensitivity. This effectively avoids the negative impact of low-sensitivity regions on both inversion efficiency and accuracy, enabling a more reliable recovery of subsurface resistivity structures in the NLCG inversion.

Due to the use of a quasi-forward modeling approach, the Jacobian matrix is not explicitly computed. Instead, we approximate sensitivity using the vector $\boldsymbol{J}^{\mathrm{T}}\boldsymbol{q}$. Given the smoother and more continuous sensitivity distribution under Dirichlet boundary conditions, we determine the inversion domain for the PML-based inversion using sensitivity results obtained from the Dirichlet setup. A tolerance threshold is defined as a small percentage of the maximum sensitivity within the survey area to identify high-sensitivity regions. Based on our inversion tests, this tolerance can be set in the range of 1%–5%. To maintain spatial continuity of the sensitivity distribution, the final inversion domain is formed by expanding a few additional grid cells beyond the high-sensitivity region.

After defining the inversion domain, the starting resistivity model for field data inversion is constructed using the average apparent resistivity of the survey area. Several nearby values are tested to ensure reasonable initialization. In CSAMT inversion, linear systems from forward and quasi-forward modeling are independent and solved in parallel using the MPI framework, which

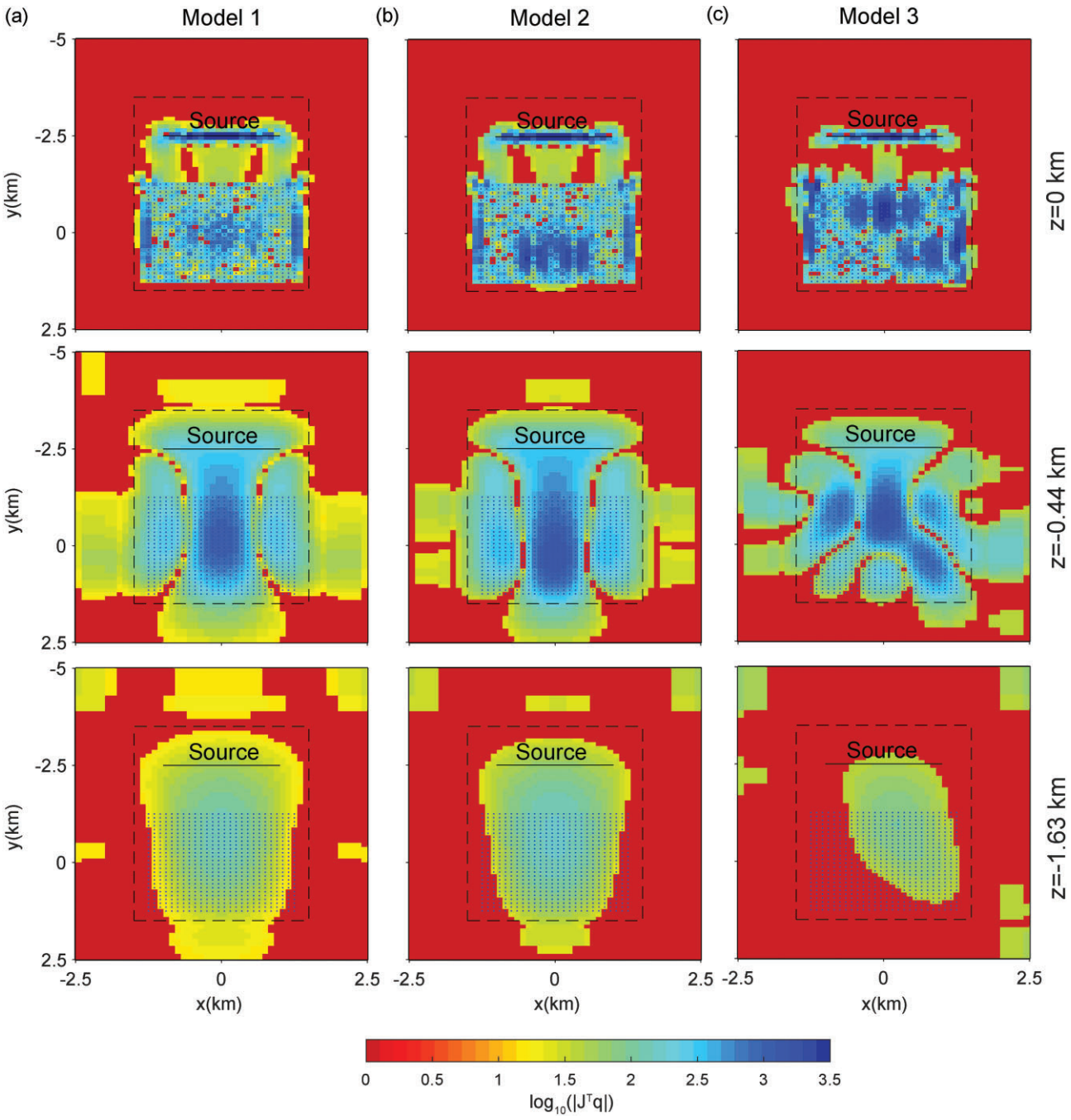

Figure 6 Plan-view distributions of $\boldsymbol{J}^{\top}\boldsymbol{q}$ using Dirichlet boundary condition exceeding a threshold (set at 1% of the maximum $\boldsymbol{J}^{\top}\boldsymbol{q}$ value beneath the survey area) at depths of $z = 0$, -0.44, and -1.63 km. The dash square outlines the inversion area used in the PML inversion. The black line represents the source, and the black points indicate the survey stations.

significantly improves computational efficiency and scalability for large-scale problems.

3. Synthetic example

In our experiments, we consider three synthetic models. A consistent discretization grid is employed across all models to evaluate the transferability of the PML parameters. In models 1–3, the transmitter is modeled as a horizontal electric dipole (HED), 2 km in length and oriented along the x-axis, with its geometric center located at (0, -2.5, and 0) km within the modeling domain. A total of 684 observation stations are uniformly distributed across the survey area, with an approximate spacing of 100 m. For consistency in comparison, the inversion domain under PML boundary conditions is defined as a spatially corresponding subset of that used with Dirichlet boundaries. All models are discretized into $46 \times 66 \times 46$ cells (including the air layer and the PML domain) for the PML scheme, and $52 \times 74 \times 40$ cells for the Dirichlet scheme.

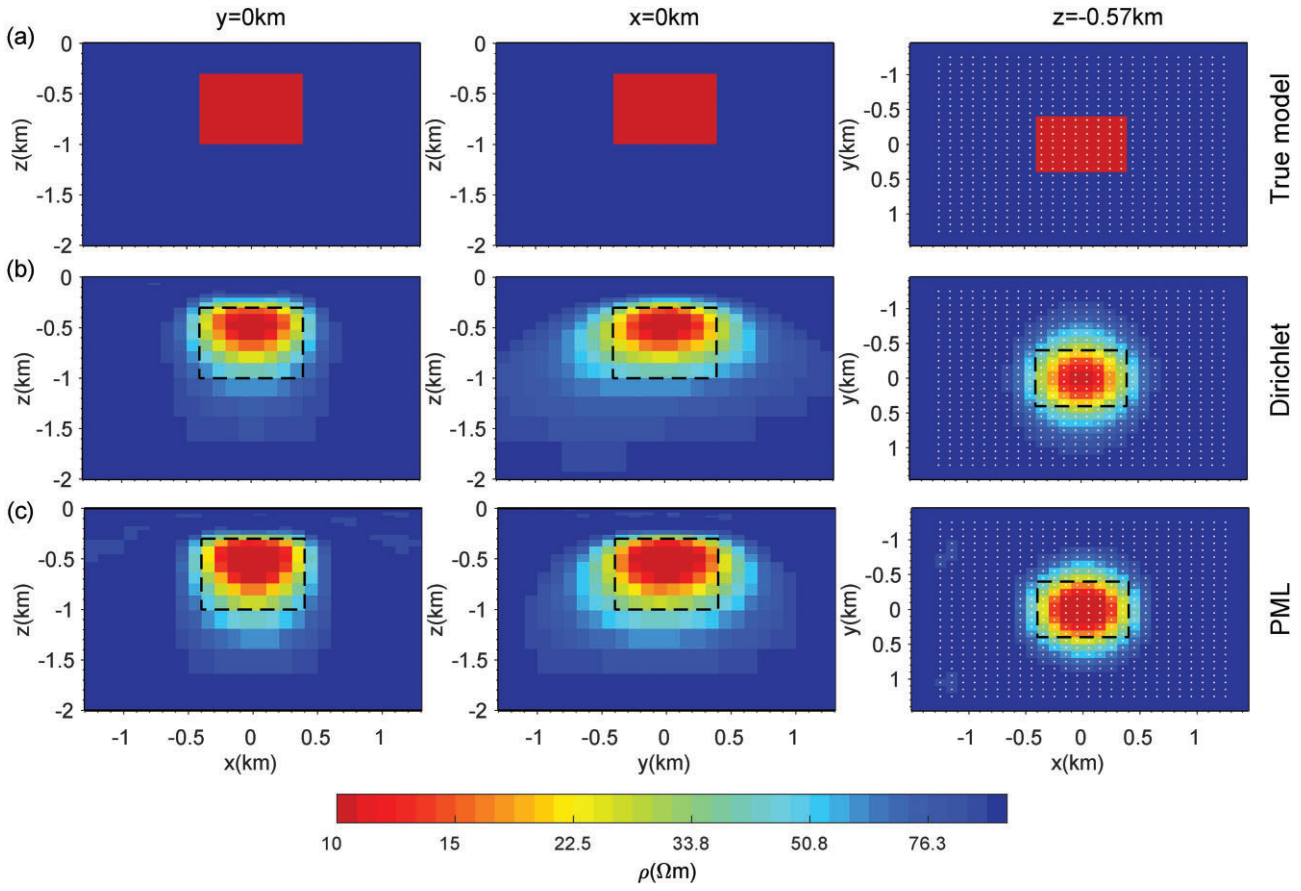

Figure 7 Inversion results for model 1. (a) The true model, (b) and (c) inversion results for model 1 using Dirichlet- and PML-based inversion schemes, respectively. The dashed box displays the outline of the target.

3.1. Synthetic model

3.1.1. Model 1

As shown in Fig. 5a, model 1 consists of a resistive prism (10 Ω m) embedded in a homogeneous half-space with a resistivity of 100 Ω m. The top of the target lies at a depth of 0.3 km, and its dimensions are 0.8 × 0.8 × 0.7 km in the *x*-, *y*-, and *z*-directions, respectively.

To absorb outgoing secondary fields, 8 PML layers are placed along the model boundaries, with each PML cell having a width of 50 m. The total number of grid cells is 46 × 66 × 46 (including the air layer and PML).

3.1.2. Model 2

Model 2, depicted in Fig. 5b, is derived from model 1 but features a stepped 10 Ω m anomaly in place of the original target. The anomaly begins at a depth of 0.13 km and extends downward to 1 km. Horizontally, it spans 0.8 km in the *x*-direction (from −0.4 to 0.4 km) and 1.6 km in the *y*-direction (from −0.7 to 0.9 km). The observation layout for model 2 is identical to that of model 1.

3.1.3. Model 3

To evaluate the performance of the inversion code in resolving multiple targets, model 3 (Fig. 5c) is designed with six block-shaped anomalies, each measuring 0.6 × 0.6 × 0.322 km. The top depth of each block is 0.198 km. The resistivities of the six targets (labeled A through F) are 1000, 1, 500, 50, 300, and 10 Ω m, respectively. The observation configuration remains the same as in model 1.

3.2. Inversion results

We determined the optimal PML parameters for model 1 across the frequency range from 8192 to 0.125 Hz. The resulting optimal values were $\kappa_{opt} = 0.77$, $\gamma_{opt} = 3.62$, and $\alpha_{opt} = 145.1$, which achieved a minimum reflection error of −114.52 dB at 8192 Hz, and a maximum of −48.81 dB at 8 Hz. To evaluate the transferability of these optimal parameters to models with different resistivity distributions but the same grid, we applied them to models 2 and 3. The minimum reflection errors were −99.23 and −83.13 dB at 8192 Hz, while the maximum reflection errors were −59.83 and −48.16 dB at 8 Hz, respectively. Although the minimum reflection errors increased slightly in models 2 and 3, all values remained well below −40 dB, indicating that the optimal PML parameters are transferable across models with identical grids. However, in inversion applications, the model resistivity is continuously updated during the iterative process. Although the grid remains unchanged, the background resistivity may vary to some extent, especially in inversions involving field data. To investigate the robustness of the optimal PML parameters under such conditions, we modified the background resistivity of model 1 to 1, 50, 500, and 1000 Ω m, and computed the corresponding reflection

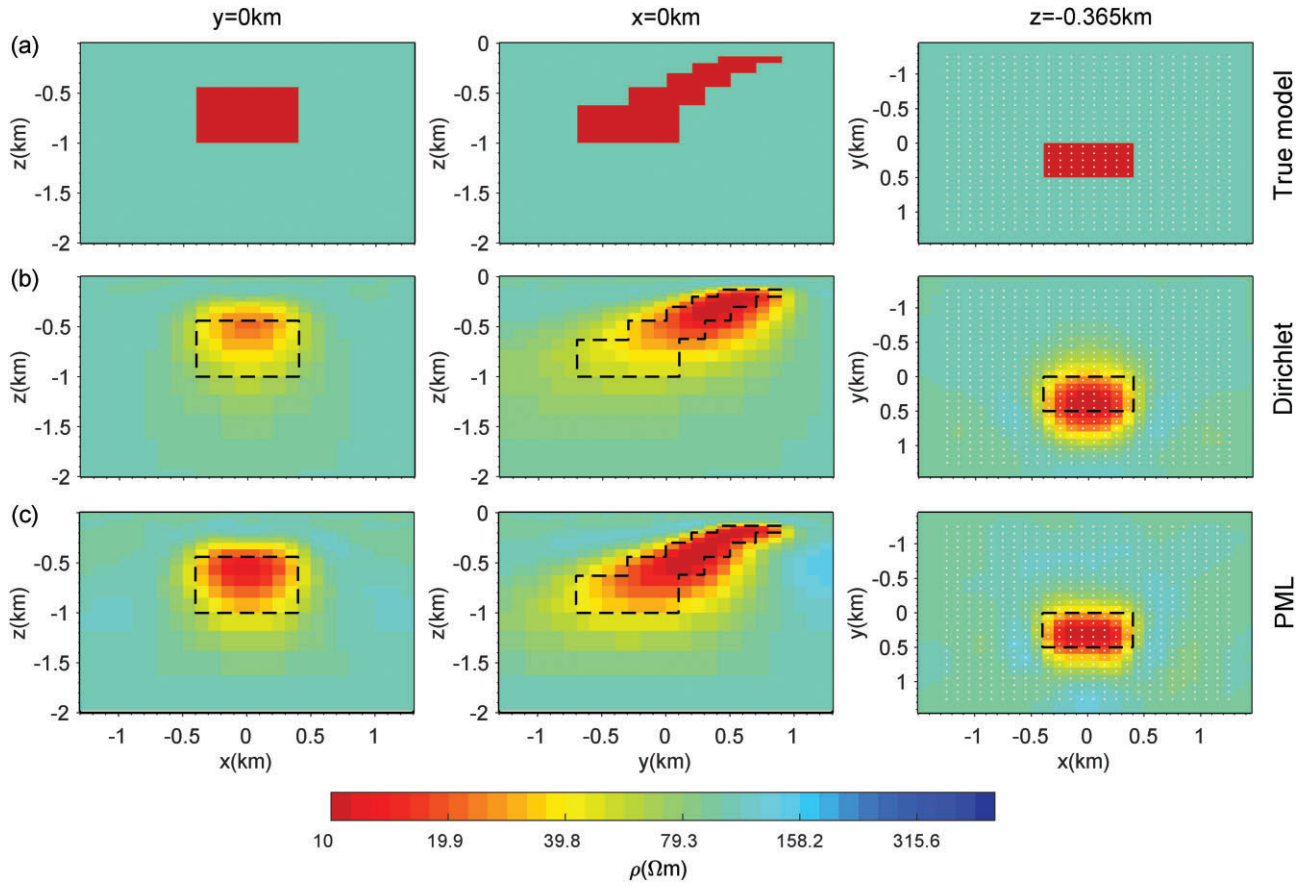

Figure 8 Inversion results for model 2. (a) The true model, (b) and (c) inversion results for model 2 using Dirichlet- and PML-based inversion schemes, respectively. The dashed box displays the outline of the target.

errors using the previously obtained optimal parameters. The minimum reflection errors were found to be −44.6, −48.26, −45.8, and −43.18 dB, respectively. All values remained below −40 dB, exhibiting a certain tolerance to variations in background resistivity within a reasonable range. These results suggest that the determined optimal PML parameters can be reliably applied in inversion processes without the need for adjustment during the iterative updates.

To generate synthetic datasets, apparent resistivity and phase were contaminated with 3% Gaussian random noise. To determine an appropriate inversion domain, we first computed the initial sensitivity—approximated by $\boldsymbol{J}^T\boldsymbol{q}$—using the model configured with Dirichlet boundary conditions. A threshold was set at 1% of the maximum $\boldsymbol{J}^T\boldsymbol{q}$ value beneath the survey area to isolate high-sensitivity regions. As illustrated in Fig. 6, the distributions of $\boldsymbol{J}^T\boldsymbol{q}$ exceeding this threshold are shown for all three models, exhibiting a general trend of decay with increasing depth. Based on this distribution pattern, and after excluding the extended regions introduced by the Dirichlet boundary condition, the final inversion domain was defined and is delineated by dashed lines in the Fig. 6.

The initial model was defined as a homogeneous half-space with a resistivity of 100 Ω m. An RMS misfit of the data threshold of 1.0 was adopted. Error floors were set to 3% for apparent resistivity and 1.5% for phase. Various initial regularization weights were tested during inversion to balance model smoothness and data fit. For performance comparison, all inversions were executed using 17 MPI processes, with each process configured to use two threads during the LU factorization step in PARDISO.

To quantitatively assess the accuracy of the inversion results, we calculated the model misfit between the true model and the inverted model. The RMS of the model perturbation is defined as (Moorkam *et al.* 2011; Zhu *et al.* 2023)

$$\zeta = \frac{1}{M_p}\sqrt{\sum_{i=1}^{M_p}\left(\frac{m_i^{inv}-m_i^{true}}{m_i^{true}}\right)^2}, \tag{10}$$

where m_i^{true} and m_i^{inv} represent the resistivity values of the true and inverted models, respectively, and M_p is the total number of grid cells within the target region. Only the cells corresponding to the target body were included in the calculation to better reflect the inversion accuracy within the area of interest.

For easier comparison of the inversion results, short-offset acquisition, the cooling strategy, and MPI techniques are also employed in the Dirichlet-based inversion implemented in this study.

3.2.1. Model 1

Figure 7 shows the inversion results of the synthetic data from model 1 using the traditional Dirichlet-based inversion and our robust PML-based inversion scheme. The RMS misfits converged from 7.03 to 1.63 for the Dirichlet-based inversion and to 1.54 for the PML-based inversion. The total inversion time was ∼30.4 h for the Dirichlet case and 12.5 h for the PML-based case,

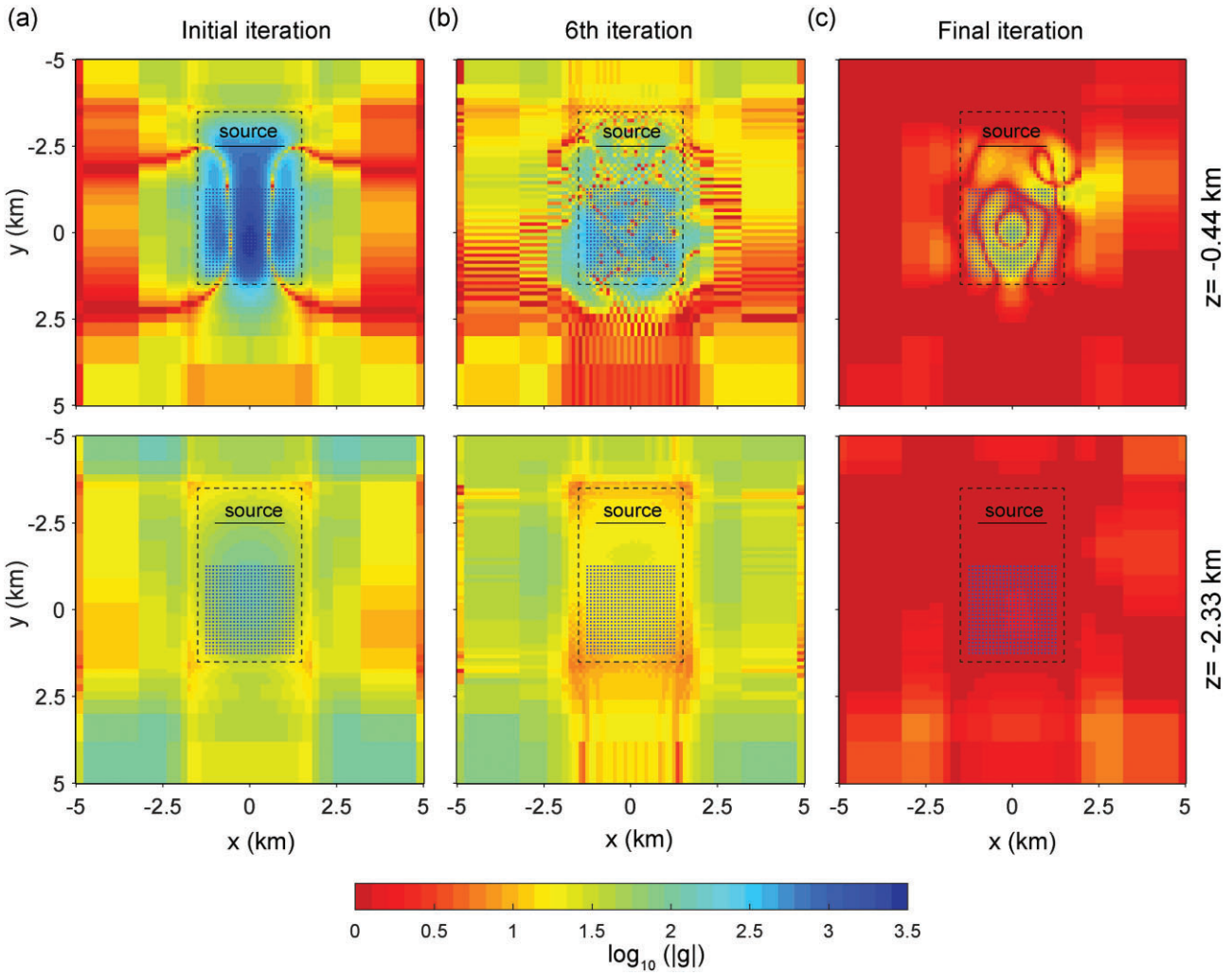

Figure 9 Plan-view distribution of gradient magnitude using Dirichlet boundary condition at depths of $z = -0.44$ and -2.33 km for the initial, sixth, and final iterations for model 2. The dash line outlines the inversion area used in PML-based inversion. The black line represents the source, and the black points indicate the survey stations.

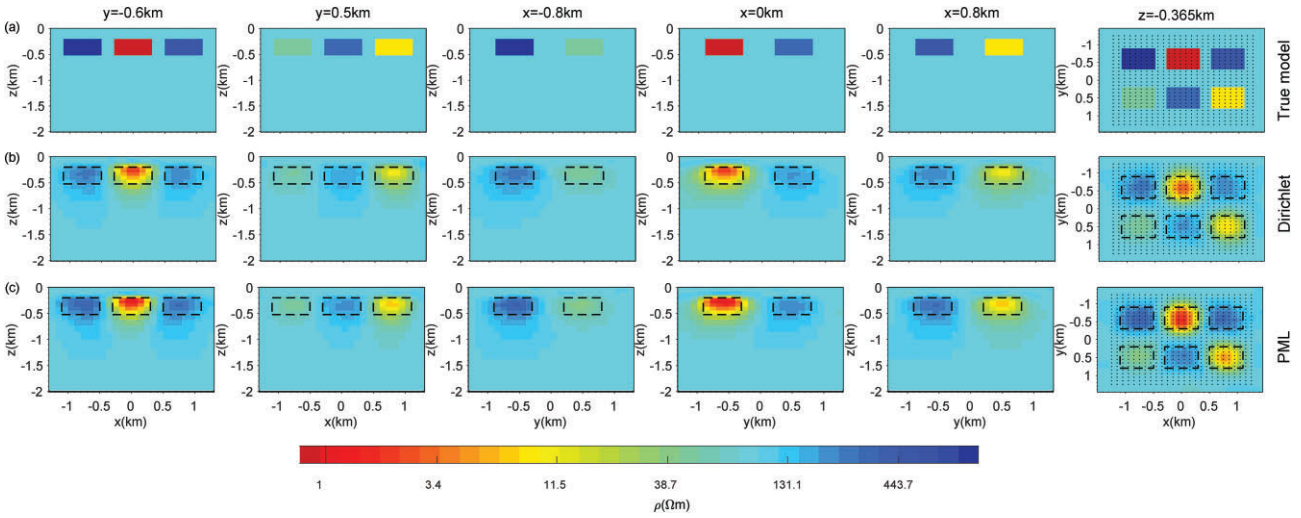

Figure 10 Inversion results for model 3. (a) The true model, (b)–(c) inversion results for model 3 using Dirichlet- and PML-based inversion schemes, respectively. The dashed box displays the outline of the target.

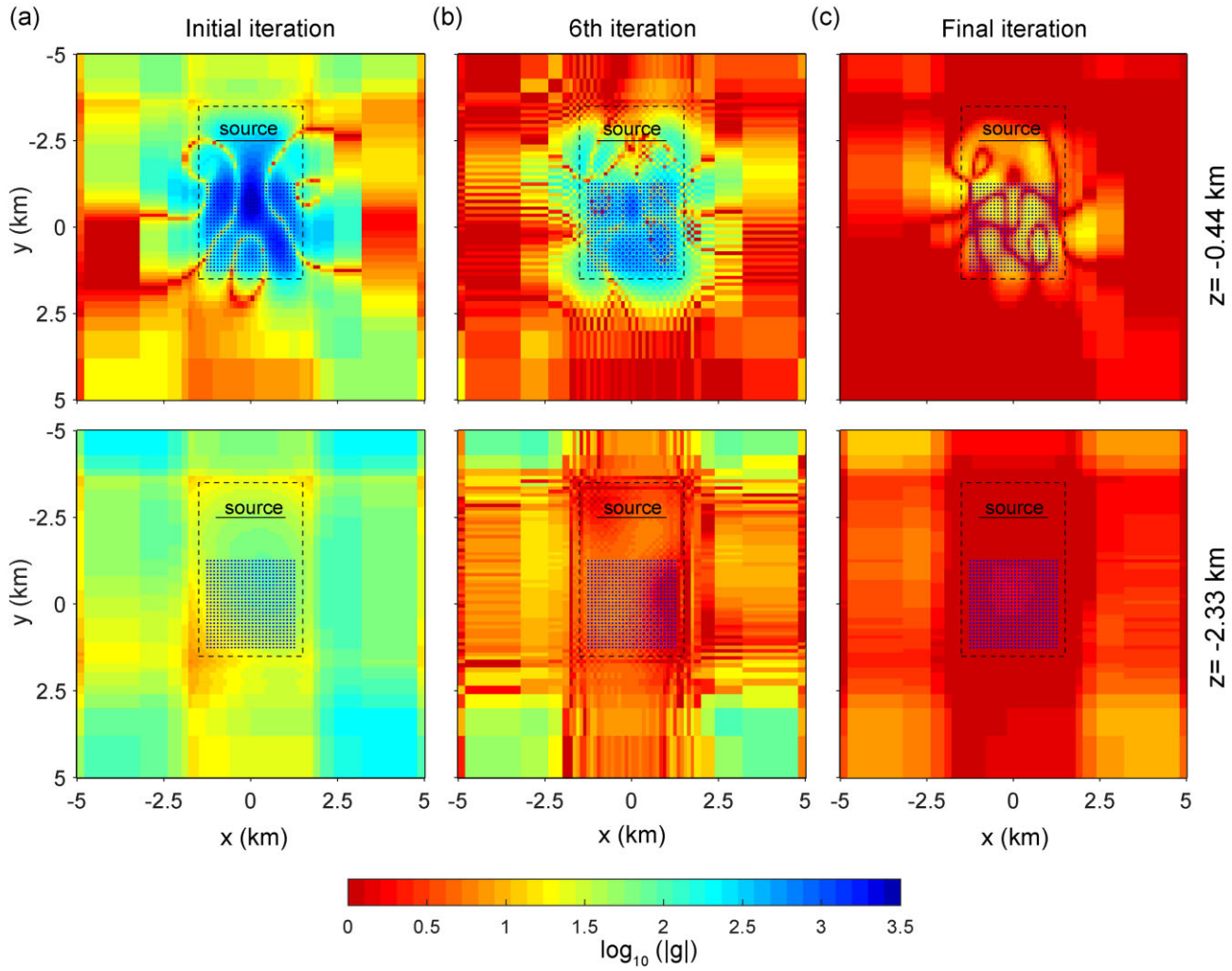

Figure 11 Plan-view distribution of gradient magnitude using Dirichlet boundary condition at depths of $z = -0.44$ and -2.33 km for the initial, sixth, and final iterations for model 3. The dash line outlines the inversion area used in PML-based inversion. The black line represents the source, and the black points indicate the survey stations.

representing a nearly 2.4-fold improvement in computational efficiency.

This improvement is primarily attributed to the reduction of the inversion domain in PML-based inversion scheme ($46 \times 66 \times 46$). The extended region required for Dirichlet boundaries ($52 \times 74 \times 40$) is eliminated, significantly decreasing the number of grid cells. Additionally, the PML-based inversion exhibited higher convergence efficiency, requiring only 44 iterations compared to 63 for the Dirichlet-based inversion, further enhancing the overall inversion efficiency.

As shown in Fig. 7, the target's position and resistivity are recovered in both cases. Notably, the inversion results obtained in PML-based inversion are nearly identical to those derived in Dirichlet-based inversion, confirming the validity of PML for inversion applications.

To quantitatively assess the deviation of the inverted models from the true model, the model perturbation RMS (ζ) was calculated. The ζ value was 0.116 for the Dirichlet-based inversion and 0.094 for the PML-based inversion, indicating that the target was more accurately recovered and the overall model accuracy was higher using the PML-based approach.

3.2.2. Model 2

Figure 8 presents the inversion results for model 2 using both Dirichlet- and PML-based schemes. After 65 and 55 iterations, the RMS misfits decreased from 9.72 to 1.73 for the Dirichlet-based inversion, and to 1.54 for PML-based inversion. The total inversion time was ~26.8 h for the Dirichlet-based inversion, while the PML-based method required only 9.86 h, representing a 2.7-fold improvement in computational efficiency.

As shown in Fig. 8, the recovered targets from both inversion results are close to the true model. However, the model perturbation RMS was lower for the PML-based inversion ($\zeta = 0.086$) compared to the Dirichlet-based case ($\zeta = 0.125$). Moreover, as shown in Fig. 8, the PML-based inversion better recovered the deeper portions of the target, likely due to improved data fitting.

To understand this difference, we analyzed the distribution of gradient magnitude using the Dirichlet boundary condition—which guide model updates—at two depth levels ($z = -0.44$ and -2.33 km) during the initial, sixth, and final iterations. Shallow-region gradients in the initial iteration as shown in Fig. 9a were mainly concentrated between the survey area and the source, while deep-region large grid cells, introduced to satisfy the

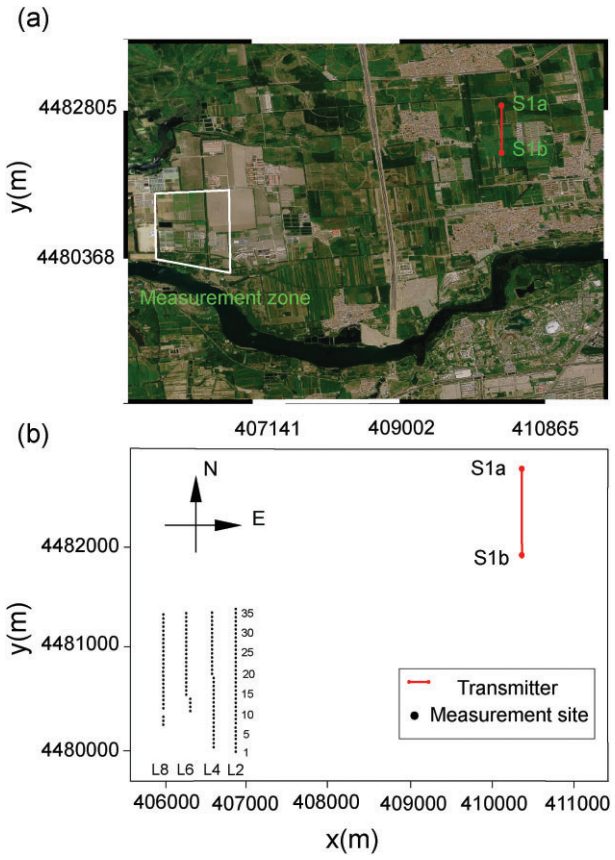

Figure 12 Survey stations and transmitters with red lines. (a) White polygon indicates the measurement zone. (b) Black point denotes the survey station.

Dirichlet boundary condition, also exhibited relatively high gradient values. Although these gradients diminished at sixth iteration, significant values persisted in the deep large cells as shown in Fig. 9b; in the final iteration, their maximum gradient still reached 12.41% of the shallow maximum at $z = -0.44$ km, as shown in Fig. 9c.

Despite the presence of high gradients in the deep large grid cells, the final resistivity changes in these areas were minimal (about 1 Ω m). This suggests that while the large cells did not directly alter the model, their gradients still entered the optimization process, potentially influencing the global update direction or step size selection. In this way, they may have indirectly hindered convergence and model accuracy.

To verify this, we conducted a supplementary experiment using Dirichlet boundary conditions but restricted the model update to the region used in the PML-based inversion. This excluded the influence of deep large cells with high gradients. As a result, the RMS misfit improved significantly (1.59), and the inversion results closely aligned with those obtained from our scheme, confirming the detrimental effect of including such cells in the update region.

By limiting inversion to high-sensitivity regions, the PML-based scheme avoids the adverse influence of artificial gradients, thus leading to more accurate model updates and improved convergence and inversion efficiency.

3.2.3. Model 3

Figure 10 presents the inversion results for model 3 using he traditional Dirichlet-based inversion and our proposed PML-based inversion scheme. After 71 and 73 iterations, the RMS misfits decreased from 10.36 to 1.91 for the Dirichlet-based inversion, and to 1.65 for PML-based inversion. The total inversion time was ∼30.5 h for the Dirichlet case, compared to 15.16 h for PML-based inversion. Although our scheme required slightly more iterations, it achieved a lower RMS misfit and significantly reduced computational time. This improvement is attributed not only to the reduced number of grid cells, but also to fewer line searches required during the optimization process.

As shown in Fig. 10, all six targets were successfully recovered in both inversion results. However, a comparison reveals that the resistivity values of targets A and F obtained using the PML-based scheme (Fig. 10c) are more accurate than those from the Dirichlet-based result (Fig. 10b). For the remaining targets, the differences are relatively minor.

To quantify these observations, we calculated the model perturbation RMS for each target (A–F). The RMS values for the Dirichlet-based inversion are 0.060, 1.379, 0.048, 0.029, 0.034, and 0.159, respectively, whereas those from the PML-based scheme are 0.056, 1.195, 0.043, 0.023, 0.029, and 0.129. These results demonstrate that the PML-based scheme consistently achieves lower perturbation errors across all targets, indicating higher model recovery accuracy.

Similar to model 2, we analyzed the distribution of gradient magnitudes at two depth levels ($z = -0.44$ km and $z = -2.33$ km) during the initial, sixth, and final iterations (Fig. 11). By the sixth iteration, the RMS misfit had already decreased to 4.6. The evolution of the gradient distribution follows a similar pattern as in model 2, further confirming that large grid cells under Dirichlet conditions can adversely affect convergence behavior during inversion.

4. Field example

4.1. The survey

The field CSAMT data set was collected from the Yanqing area, situated in the northern part of Beijing, a region notable for its rich geothermal resources. A brief overview of the survey layout is provided here, while detailed descriptions can be found in Wang & Lin (2025). The scalar dataset consists of 122 stations acquiring from a GDP32-II system, with signal frequencies ranging from 8192 to 0.25 Hz. As illustrated in Fig. 12, four survey lines—designated as Lines 2, 4, 6, and 8—were deployed across the area. The spacing between adjacent stations along each north–south profile is ∼40 m. The source, aligned parallel to the survey lines, was an 824.6-m-long HED transmitter. The distance between the source and line 2 was 3508.9 m.

4.2. The inversion settings

The dataset was first processed using Zonge software packages SHRED, AMTAVG, and SCS2D, followed by 3D CSAMT inversion. Topography was not incorporated in the inversion since the survey was conducted in the Yanqing Plain, where elevation changes are less than 10 m. The starting model is the same as that used by Wang & Lin (2025), consisting of a homogeneous half-space with a resistivity of 35 Ω m. Error floors were set at 15% for apparent resistivity and 7.5% for phase, with an RMS misfit threshold of 1.0. To determine a suitable inversion model, initial regularization parameters ranging from 100 to 100 000 were tested.

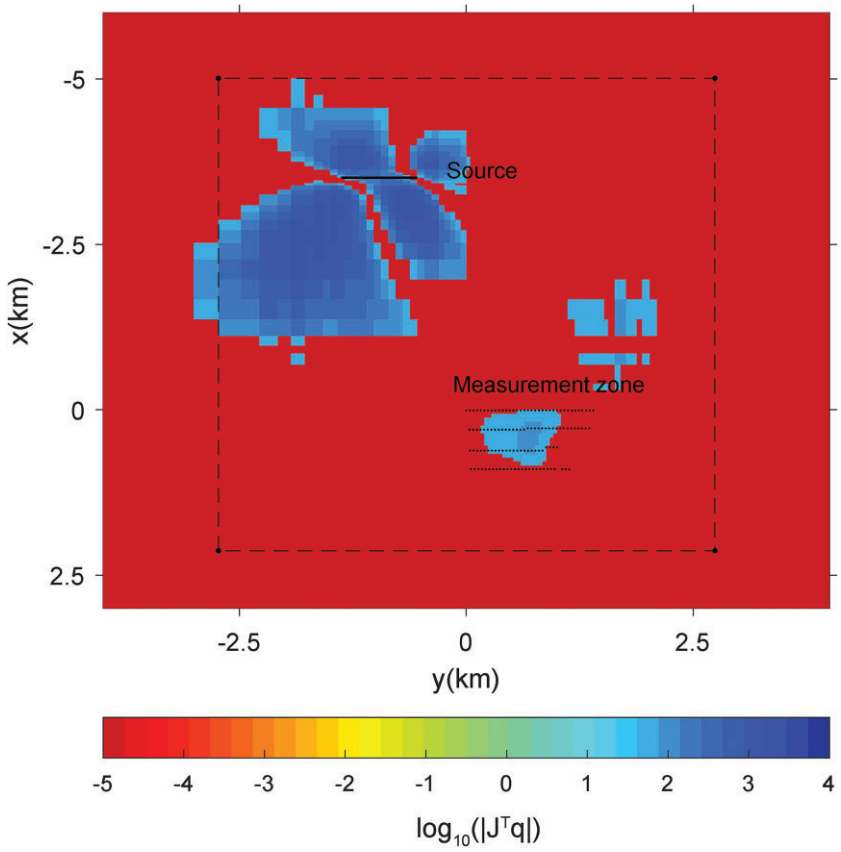

Figure 13 Plan-view distributions of $\boldsymbol{J}^{\top}\boldsymbol{q}$ using Dirichlet boundary condition exceeding a threshold (set at 1% of the maximum $\boldsymbol{J}^{\top}\boldsymbol{q}$ value beneath the survey area) at depths of $z = -0.37$ km. The dash square outlines the inversion area used in PML-based inversion. The black line represents the source, and the black points indicate the survey stations.

For the inversion grid cells in PML-based inversion, the inversion domain was carefully designed based on initial data sensitivity analysis with the Dirichlet boundary condition. To delineate the high-sensitivity region, we selected initial $\boldsymbol{J}^{\top}\boldsymbol{q}$ values greater than 1% of the maximum value observed within the survey area under Dirichlet boundary conditions. Figure 13 shows the distribution at a depth of 370 m. It can be observed that the initial data sensitivity is particularly high in the region between the source and the measurement area, and this sensitive region lies very close to the measurement zone. After excluding the extended regions introduced by the Dirichlet boundary condition, by balancing both data sensitivity and inversion efficiency, we defined the inversion domain under the PML boundary condition as the area enclosed by the black box shown in the Fig. 13. An additional reason for including the source within the inversion domain is its close proximity to the survey zone, which may give rise to strong stratigraphic waves and potential source overprint or shadow effects in field data inversion (Lei *et al.* 2016).

The inversion region, where model updates are permitted, spans from −2.74 to 2.74 km in the x-direction and from −5.01 to 2.13 km in the y-direction. Within the measurement area, the grid cell sizes in the x- and y-directions were set to 40 and 60 m, respectively, and increase gradually to a maximum of 250 m outward. In the z-direction, the cell thickness starts from 10 m near the surface and increases progressively, reaching a maximum depth of 13 km. Eight PML layers are placed outside the inversion domain. The subsurface was discretized into a total of 100 × 86 × 54 grid cells, including the PML and air layers.

To find the κ_{opt}, γ_{opt}, and α_{opt}, we set a 1 Ω m prism below the measurement zone with 1.64 × 1.08 × 0.653 km and a top depth of 95 m. The background resistivity is 35 Ω m. the PML parameter is $\kappa_{opt} = 1.36$, $\gamma_{opt} = 2.96$, and $\alpha_{opt} = 42.17$, with a minimum reflection error of −49.6 dB.

In the inversion, four MPI processes were used, with 40 threads allocated for LU factorization via PARDISO. The PML-based inversion required a total of 45.66 h. The RMS data misfit decreased from 7.26 to 1.1. The inversion results are presented in Fig. 14e–h. For comparison, the inversion result using the Dirichlet boundary condition, obtained by Wang & Lin (2025), is shown in Fig. 14a–d; however, the color scale has been adjusted, and the RMS misfit reduced to 1.21.

4.3. 3D inversion results

Figures 15 and 16 show a comparison between the measured data and the predicted responses from the best-fitting models shown in Fig. 14a–d (Dirichlet-based) and 14e–14h (PML-based), respectively. The RMS misfit at each survey station is also provided. Overall, the key features of the measured data are well reproduced by both inversion results. As seen in Figs 15c and 16c, the RMS misfits at most survey stations are close to 1, with only a few exceptions. On line 8, within the 0.08–0.72 km range, the RMS misfit values in

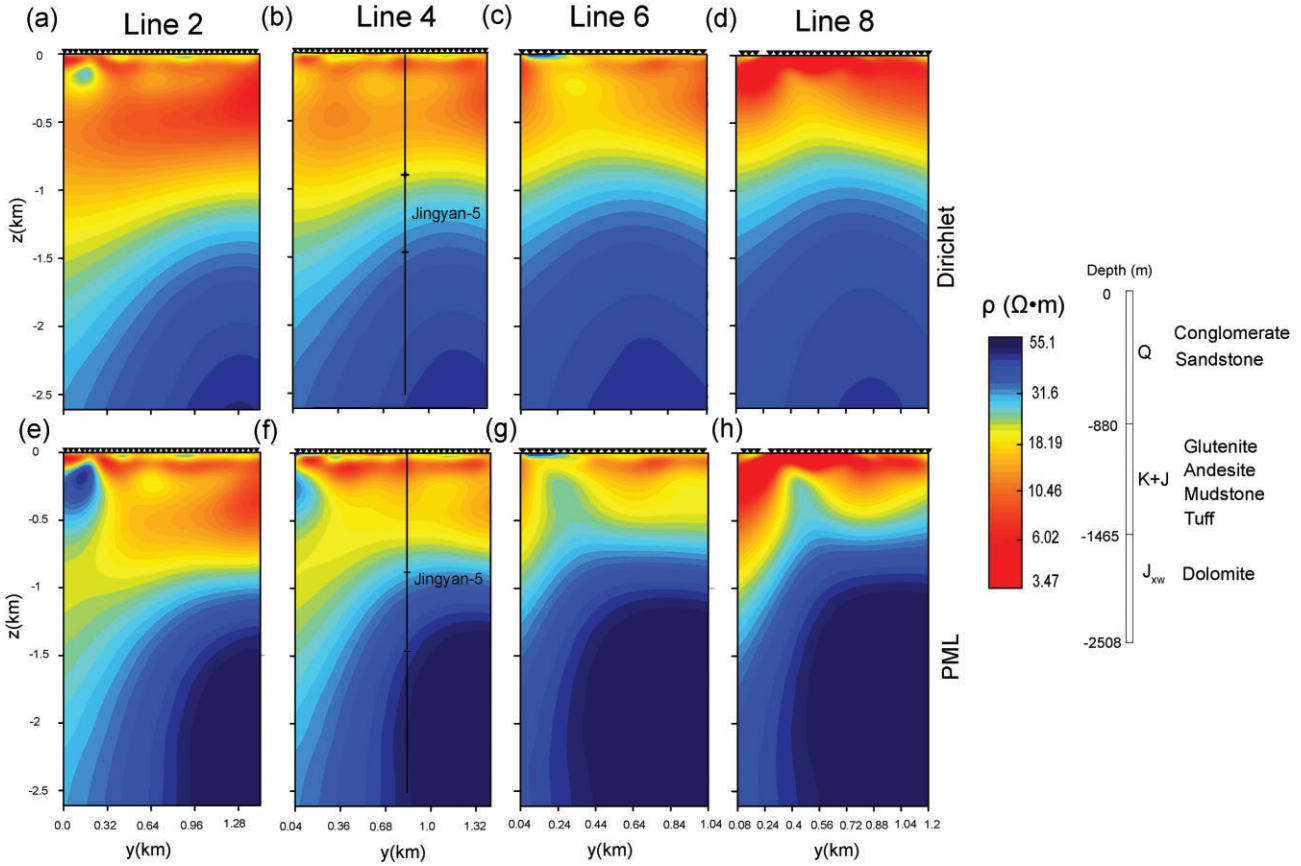

Figure 14 Sections of the 3D inversion results for using Dirichlet-based (a–d) and PML-based schemes (e–h). The solid black line depicts the borehole JingYan-5 log and its values also are presented in this figure.

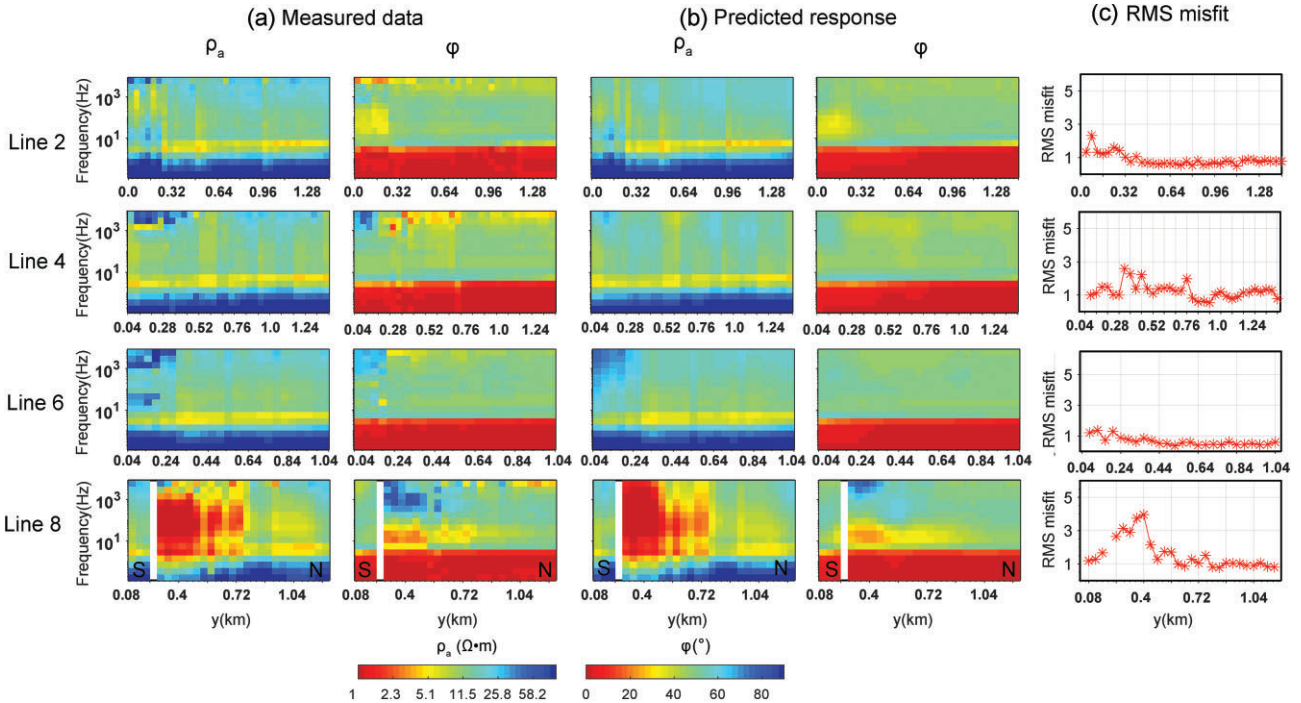

Figure 15 Comparation between the measured CSAMT data and the forward modeling of the inversion results using the Dirichlet scheme. (a) Pseudosection of the measured CSAMT data along four survey lines. (b) Responses to the inversion model in Fig. 14a–d. (c) Final RMS misfit at each site in four lines. White areas in (a) and (b) represent bad or missing CSAMT data.

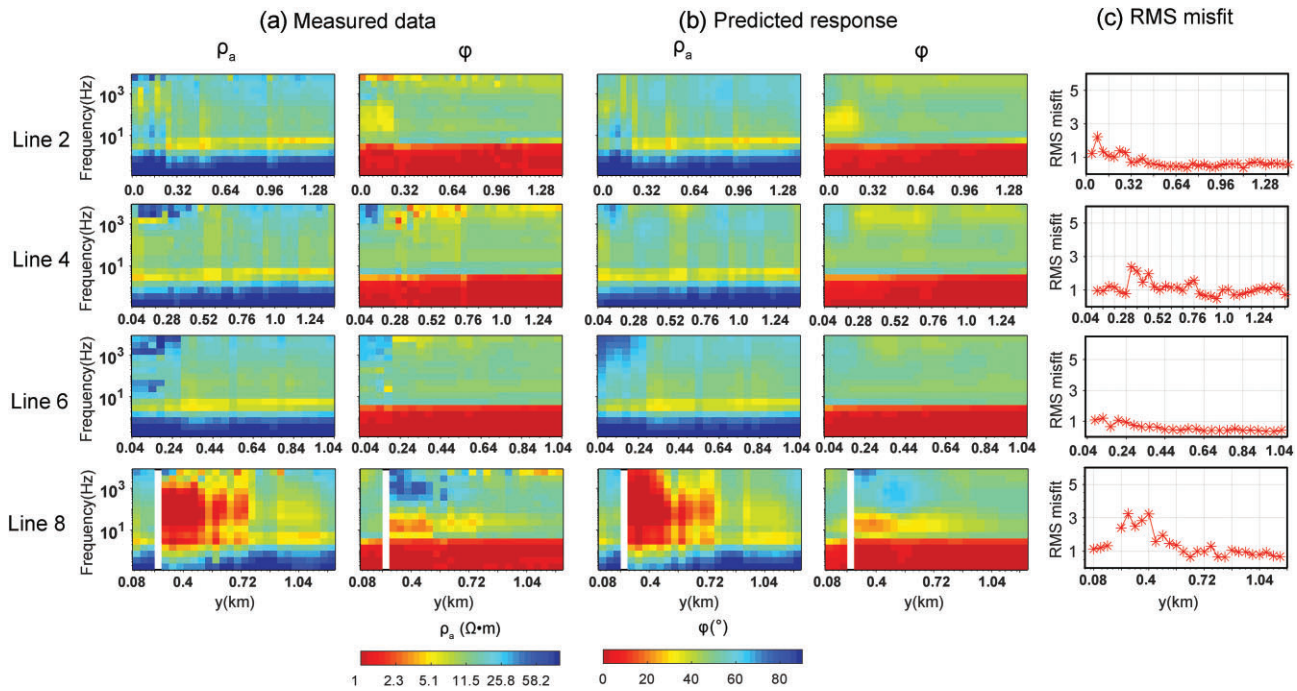

Figure 16 Comparation between the measured CSAMT data and the forward modeling of the inversion results using the PML scheme. (a) Pseudosection of the measured CSAMT data along four survey lines. (b) Responses to the inversion model in Fig. 14e–h. (c) Final RMS misfit at each site in four lines. White areas in (a) and (b) represent bad or missing CSAMT data.

Fig. 16c show a noticeable decrease, which is also reflected in the improved phase response alignment with the measured data. A close fit to the data generally implies a more reliable inversion outcome. Furthermore, the predicted responses in Figs 15b and 16b are highly consistent with one another.

The inversion results using both Dirichlet- and PML-based schemes, as depicted in Fig. 14a–d and e–14h, respectively, reveal the subsurface electrical structure beneath the measurement zone of interest. Both approaches resolve a three-layer structure: a shallow conductive layer, an intermediate resistive layer, and a deeper high-resistivity zone—broadly consistent with the lithological interpretation from borehole JingYan-5.

Geological studies have established that the area consists of a three-layer sedimentary sequence comprising the Quaternary (Q), Jurassic (J), and Cretaceous (K) formations, underlain by the Wumishan Formation of the Jixian (J_{xw}) system (Zhang 2002; Ke 2009; Lei *et al.* 2014; Sun *et al.* 2019; Zhang 2019). Integrating this geological context with borehole JingYan-5, located along line 4 (Figs 15c and 16c), suggests that the shallow low-resistivity layer corresponds to Quaternary sandstones and conglomerates. The intermediate layer likely represents Jurassic and Cretaceous tuff, mudstone, andesite, and glutenite. The deeper high-resistivity zone is attributed to the dolomite of the Wumishan Formation.

The recovered resistivity values of the top layer are nearly identical between the two inversion schemes. However, the second and third layers in the PML-based inversion (Fig. 14e–h) exhibit higher resistivity than those in the Dirichlet-based results (Fig. 14a–d). This discrepancy may be primarily due to the superior data fitting achieved with the PML-based inversion, consistent with the trends observed in the synthetic models.

Additionally, under Dirichlet boundary conditions, extended grid blocks outside the primary target region may exhibit non-negligible data sensitivity and gradient values. Consequently, these blocks can be updated during the inversion process, even though they lie far from the survey lines. From an optimization standpoint, this behavior is driven by the local gradients of the misfit function, which indicate the regions where parameter adjustments most effectively reduce the objective function. However, such a redistribution of sensitivity and gradient magnitude may shift the inversion focus away from the survey area, potentially degrading the resolution and accuracy of the recovered resistivity beneath the lines of interest. In contrast, the PML-based inversion confines model updates to genuinely high-sensitivity regions. By avoiding the influence of artificial gradients in less sensitive or non-essential areas, it enhances inversion focus and improves the reliability of the final results.

Although no direct resistivity logging was performed in borehole JingYan-5, nearby borehole Yanre-6—situated within the same structural unit—exhibits apparent resistivity values ranging from 40 to 900 Ω m in the Wumishan Formation, indicating a high-resistivity geological unit (Niu 2013). While these values reflect apparent rather than true resistivity, they suggest that the third layer in the inversion model should exhibit relatively high resistivity. Therefore, the PML-based inversion, which yields higher resistivity values in the deep layer, offers a more realistic representation of the subsurface structure.

5. Conclusions

A robust 3D NLCG inversion scheme is proposed for large-scale CSAMT data, incorporating four key enhancements to improve inversion stability, efficiency, and resistivity recovery: (i) short-offset acquisition is employed to reduce the inversion domain; (ii) a PML-based forward modeling approach is incorporated into the inversion process; (iii) a cooling strategy for the regularization factor

λ is introduced to ensure optimal inversion performance; and (iv) the inversion domain is confined to high-sensitivity regions.

3D synthetic data for three models were inverted to evaluate the scheme. The results indicate that the proposed PML-based inversion scheme is more time-efficient than the conventional Dirichlet-based scheme. Moreover, it exhibits higher convergence efficiency, further enhancing overall inversion performance. Importantly, in contrast to the conventional scheme, the proposed scheme yields better-defined resistivity models, with particularly improved recovery of target resistivity values and boundaries, especially for deep targets, due to the lower RMS misfit.

These findings are further supported by the inversion of field data from the Yanqing geothermal area. The proposed scheme produces resistivity models that better reflect the geological reality in deeper layers and show improved agreement with borehole data, achieving superior data fitting compared to the conventional approach.

Acknowledgements

This study has been supported by China Scholarship Council, and the High-Performance Computing Platform of China University of Geosciences (Beijing).

Conflict of interest statement

None declared.

Funding

This study was supported by the Deep Earth Probe and Mineral Resources Exploration—National Science and Technology Major Project of China (grant nos. 2024ZD1002800), and the National Natural Science Foundation of China (grant nos. 41674134 and 41874159).

Data availability

Data associated with this research are available and can be obtained by contacting the corresponding author.

References

Boerner DE, Wright JA, Thurlow JG, Reed LE. 1993. Tensor CSAMT studies at the Buchans Mine in central Newfoundland. *Geophysics*, **58**:12–9. https://doi.org/10.1190/1.1443342

Cao H, Wang K, Wang X, Duan C, Lan X, Luo W, Zhang Z. 2021. Tipper data forward modelling and inversion of three-dimensional tensor CSAMT. *J Appl Geophys*, **193**:104432. https://doi.org/10.1016/j.jappgeo.2021.104432

Chave AD. 1983. Numerical integration of related Hankel transforms by quadrature and continued fraction expansion. *Geophysics*, **48**:1671–86. https://doi.org/10.1190/1.1441448

Chen M, Yan S. 2005. Analytical study on field zones, record rules, shadow and source overprint effects in CSAMT exploration. *Chin J Geophys (in Chinese)*, **48**:951–8. https://doi.org/10.3321/j.issn:0001-5733.2005.04.031

Chen X, Liu Y, Yin C, Li Y. 2020. Three-dimensional inversion of controlled-source audio-frequency magnetotelluric data based on unstructured finite-element method. *Appl Geophys*, **17**:349–60. https://doi.org/10.1007/s11770-020-0812-z

Christensen NB. 2014. Sensitivity functions of transient electromagnetic methods. *Geophysics*, **79**:E167–82. https://doi.org/10.1190/geo2013-0364.1

Commer M, Newman GA. 2009. Three-dimensional controlled-source electromagnetic and magnetotelluric joint inversion. *Geophys J Int*, **178**:1305–16. https://doi.org/10.1111/j.1365-246X.2009.04216.x

Correia D, Jin J. 2005. On the development of a higher-order PML. *IEEE Trans Antennas Propag*, **53**:4157–63. https://doi.org/10.1109/TAP.2005.859901

Di Q, Xu G, Yin C *et al.* 2020. A new method of artificial source electromagnetic detection in China. *Sci Sin Terrae*, **50**:1219–27. https://doi.org/10.1360/SSTe-2019-0162

Feng D, Wang X. 2017. Convolution perfectly matched layer for the finite-element time-domain method modelling of ground penetrating radar (in Chinese). *Chin J Geophys (in Chinese)*, **60**:413–23. https://doi.org/10.6038/cjg20170134

Gedney SD. 1996. An anisotropic perfectly matched layer-absorbing medium for the truncation of FDTD lattices. *IEEE Trans Antennas Propag*, **44**:1630–9.

Haber E, Ascher UM, Oldenburg D. 2000. On optimization techniques for solving nonlinear inverse problems. *Inverse Prob*, **16**:1263–80. https://doi.org/10.1088/0266-5611/16/5/309

He L, Wang J, Bai H, Liu Z. 2019. A novel parallel and distributed magnetotelluric inversion algorithm on multi-threads workloads cluster. *Cluster Computing*, **22**:1073–83. https://doi.org/10.1007/s10586-018-2864-x

Jia R, Groom RW. 2013. Application of 3D CSAMT inversion to various data components and its enhancement. *Proc Symp Appl Geophys Eng Environ Probl*, **30**:30–8. https://doi.org/10.4133/sageep2013-024.1

Ke B. 2009. Geothermal and geological features of Sunhe fault in the northern part of Beijing plain. *Geoscience*, **23**:43–3. https://doi.org/10.3969/j.issn.1000-8527.2009.01.007

Kelbert A, Meqbel N, Egbert GD, Tandon K. 2014. ModEM: a modular system for inversion of electromagnetic geophysical data. *Comput Geosci*, **66**:40–53. https://doi.org/10.1016/j.cageo.2014.01.010

Kong W, Tan H, Lin C, Unsworth M, Lee B, Peng M, Wang M *et al.* 2021. Three-dimensional inversion of magnetotelluric data for a resistivity model with arbitrary anisotropy. *J Geophys Res: Solid Earth*, **126**:e2020JB020562. https://doi.org/10.1029/2020JB020562

Kouadio LK, Xu Y, Liu C, Boukhalfa Z. 2020. Two-dimensional inversion of CSAMT data and three-dimensional geological mapping for groundwater exploration in Tongkeng Area, Hunan Province, China. *J Appl Geophys*, **183**:104204. https://doi.org/10.1016/j.jappgeo.2020.104204

Lei D, Wu X, Di Q, Wang G, Lv X, Wang R, Yang J *et al.* 2016. Modelling and analysis of CSAMT field source effect and its characteristics. *J Geophys Eng*, **13**:49–58. https://doi.org/10.1088/1742-2132/13/1/49

Lei X, Guan W, Guo G, Zhu L. 2014. Application of CSAMT in the survey of karst water in the eastern Yanqing basin of Beijing. *Geotech Investig Surv*, **5**:89–98. https://doi.org/CNKI:SUN:GCKC.0.2014-05-021

Li G, Li Y, Han B, Liu Z. 2018. Application of the perfectly matched layer in 3-D marine controlled-source electromagnetic modelling. *Geophys J Int*, **212**:333–44. https://doi.org/10.1093/gji/ggx382

Li H, Yin H, Gao W, Xiao P. 2025. 3D inversion of controlled-source electromagnetic data for coalbed methane exploration in southern Yanchuan. *Pure Appl Geophys*, **182**:2153–67. https://doi.org/10.1007/s00024-025-03699-x

Lin C, Tan H, Shu Q, Tong T, Tan J. 2012. Three-dimensional conjugate gradient inversion of CSAMT data. *Chin J Geophys (in Chinese)*, **55**:3829–38. https://doi.org/10.6038/j.issn.0001-5733.2012.11.030

Lin C, Tan H, Wang W, Tong T, Peng M, Wang M, Zeng W. 2018. Three-dimensional inversion of CSAMT data in the presence of topography. *Explor Geophys*, **49**:253–67. https://doi.org/10.1071/EG16067

Liu L, Zhu F, Xu C, Niu D, Qiu R. 2013. Implementation of perfect conductor boundary condition for FDTD method truncated with calculation domain of symmetric structures. *Opto-Electron Eng*, **40**:56–61.

Mackie R, Soyer W, Miorelli F, Schifano V, Hallinan S. 2020. True 3D modelling of land controlled source EM. *SEG Tech Program Expand Abstr*, **1394**:1394–8.

Moorkamp M, Heincke B, Jegen M, Roberts AW, Hobbs RW. 2011. A framework for 3-D joint inversion of MT, gravity and seismic refraction data. *Geophys J Int*, **184**:477–93. https://doi.org/10.1111/j.1365-246X.2010.04856.x

Nabighian MN. 1991. *Electromagnetic Methods in Applied Geophysics: Volume 2, Application, Parts A and B*. Tulsa, OK: SEG.

Newman GA, Alumbaugh DL. 2000. Three-dimensional magnetotelluric inversion using non-linear conjugate gradients. *Geophys J Int*, **140**:410–24. https://doi.org/10.1046/j.1365-246x.2000.00007.x

Niu S. 2013. *Research on the geothermal development in Sanlihe District*. MS Thesis, Yanqing County, Beijing City: China Univ Geosci Beijing.

Nocedal J, Wright SJ. 2006. *Numerical Optimization*. New York, NY: Springer.

Pellerin L, Johnston JM, Hohmann GW. 1996. A numerical evaluation of electromagnetic methods in geothermal exploration. *Geophysics*, **61**:121–30. https://doi.org/10.1190/1.1443931

Peng R, Zhou W, Hu X, Liao W, Wei M, Zhang C. 2023. 3D inversion of multifrequency controlled-source electromagnetic data and its application to geothermal exploration in the Tianzhen region of the northern Datong Basin, China. *Geophysics*, **88**:E173–87. https://doi.org/10.1190/geo2022-0659.1

Sun Z, He T, Niu S. 2019. Characteristics and utilization of geothermal resource in Sanlihe area of Yanqing District, Beijing. *Urban Geol*, **14**:37–42.

Tikhonov AN, Arsenin VY. 1977. *Solutions of Ill-posed Problems*. Washington, DC: Winston & Sons.

Unsworth MJ, Bryan JT, Alan DC. 1993. Electromagnetic induction by a finite electric dipole source over a 2-D earth. *Geophysics*, **58**:198–214. https://doi.org/10.1190/1.1443406

Unsworth MJ, Lu X, Watts MD. 2000. CSAMT exploration at Sellafield: characterization of a potential radioactive waste disposal site. *Geophysics*, **65**:1070–9. https://doi.org/10.1190/1.1444800

Wang S, Lin C. 2025. New advance in land controlled-source audio-frequency magnetotellurics exploration: measurement at a shortened transmitter-receiver offset and three-dimensional inversion. *IEEE J Sel Top Appl Earth Obs Remote Sens*, **18**:12224–40. https://doi.org/10.1109/JSTARS.2025.3564862

Wang T, Wang K, Tan H. 2017. Forward modelling and inversion of tensor CSAMT in 3D anisotropic media. *Appl Geophys*, **14**:590–605. https://doi.org/10.1007/s11770-017-0644-7

Wannamaker PE. 1997. Tensor CSAMT survey over the Sulphur Springs thermal area, Valles Caldera, New Mexico, United States of America, Part I: implications for structure of the western caldera. *Geophysics*, **62**:451–65. https://doi.org/10.1190/1.1444156

Ward SH, Hohmann GW. 1988. Geophysical electromagnetic theory. In: MN Nabighian (ed.), *Electromagnetic Methods in Applied Geophysics, Vol. 1, Theory*. Tulsa, OK: SEG.

Yang L, Lei D, Di Q. 2021. A perfectly matched layer metric for the electromagnetic diffusion field. *IEEE Trans Antennas Propag*, **69**:928–39. https://doi.org/10.1109/TAP.2020.3008614

Zhang C. 2002. Research on ground thermal water resources in north part of Yanqing county, Beijing City. *Coal Geol China*, **14**:39–41. https://doi.org/10.3969/j.issn.1674-1803.2002.03.016

Zhang J. 2019. Analysis on geothermal geology characteristics in the northwest of Yanqing District, Beijing. *Urban Geol*, **14**:26–33. https://doi.org/10.3969/j.issn.1007-1903.2019.01.005

Zhu D, Tan H, Peng M, Wang T. 2023. Three-dimensional joint inversion of the resistivity method and time-domain-induced polarization based on the cross-gradient constraints. *Appl Sci*, **13**:8145. https://doi.org/10.3390/app13148145

Received: 28 October 2025. **Revised:** 28 January 2026. **Accepted:** 1 March 2026